



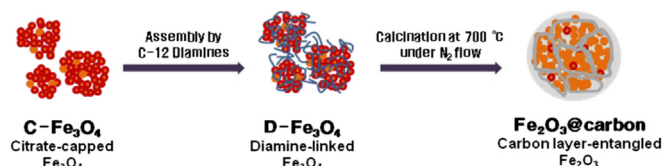
## Short communication

Facile synthesis of carbon layer-entangled  $\text{Fe}_2\text{O}_3$  clusters as anode materials for improved Li-ion batteriesHang-Deok Oh <sup>a</sup>, Sang-Wha Lee <sup>a,\*</sup>, Sang-Ok Kim <sup>b</sup>, Joong Kee Lee <sup>b,\*\*</sup><sup>a</sup> Department of Chemical and Biochemical Engineering, Gachon University, Seongnam-si, Gyeonggi-do, Republic of Korea<sup>b</sup> Advanced Energy Materials Processing Laboratory, Battery Research Center, Korea Institute of Science and Technology, Seoul, Republic of Korea

## HIGHLIGHTS

- Carbon layer-entangled iron oxides ( $\text{Fe}_2\text{O}_3@\text{carbon}$ ) were facilely prepared.
- 1,12-Diaminododecane (C-12 diamine) induced the assembly of iron oxide clusters.
- Entangled carbon layer enhanced the conductivity and structural integrity of  $\text{Fe}_2\text{O}_3$ .
- Composite electrodes improved the electrochemical performance of Li-ion batteries.

## GRAPHICAL ABSTRACT



## ARTICLE INFO

## Article history:

Received 17 November 2012

Received in revised form

7 January 2013

Accepted 18 January 2013

Available online 29 January 2013

## Keywords:

Li-ion batteries

Anode materials

Diamine

Iron oxides

Carbon layer

## ABSTRACT

Carbon layer-entangled iron oxides ( $\text{Fe}_2\text{O}_3@\text{carbon}$ ) are facilely prepared through the cross-linking assembly of iron oxides induced by the addition of 1,12-diaminododecane (C-12 diamines). The calcined  $\text{Fe}_2\text{O}_3@\text{carbon}$  composites exhibit the XRD patterns attributed to hexagonal phase of hematite ( $\alpha\text{-Fe}_2\text{O}_3$ ) with negligible magnetism. As anode electrode materials for Li-ion batteries, the  $\text{Fe}_2\text{O}_3@\text{carbon}$  exhibits the retained capacity of  $614 \text{ mAh g}^{-1}$  at 0.1 C after 35 cycles, while the carbon free  $\text{Fe}_2\text{O}_3$  exhibits the retained capacity of  $283 \text{ mAh g}^{-1}$  at 0.1 C after 35 cycles. The unique formation of carbon layer entanglement within iron oxide clusters contributes the improved capacity retention capability of the composite electrode ( $\text{Fe}_2\text{O}_3@\text{carbon}$ ) by providing buffering space for large volume expansion and enhanced electrical conductivity between the active iron oxides.

© 2013 Elsevier B.V. All rights reserved.

## 1. Introduction

Li-ion batteries are widely employed as power sources for mobile electronics due to their high-energy density and long cycling performance [1–3]. The capacity of Li-ion batteries can be

improved by increasing the storage amounts of Li-ions in electrode materials [4,5]. Recently, transition metal oxides ( $\text{MO}_x$ ,  $\text{M} = \text{Fe, Ti, Co, Mn, etc.}$ ) have been intensively investigated as active electrode materials for Li-ion batteries because they have high theoretical specific capacity and good structural stability [6–10]. Among them, iron oxide can be an attractive anode material due to its low cost, low toxicity, and natural abundance [11,12].

Recently, hematite ( $\alpha\text{-Fe}_2\text{O}_3$ ) has been evaluated as an active anode material with the theoretical capacity of  $1007 \text{ mAh g}^{-1}$  [13–15]. The electrochemical reaction of  $\text{Fe}_2\text{O}_3$  with Li ions is given by ' $6\text{Li} + \text{Fe}_2\text{O}_3 \leftrightarrow 2\text{Fe}^0 + 3\text{Li}_2\text{O}$ ' through the intermediate complex of

\* Corresponding author. Tel./fax: +82 31 750 5360/5363.

\*\* Corresponding author. Tel./fax: +82 31 958 5252/5229.

E-mail addresses: lswha@gachon.ac.kr (S.-W. Lee), leejk@kist.re.kr (J.K. Lee).

$\text{Li}_x\text{Fe}_2\text{O}_3$  [15]. The  $\text{Fe}_2\text{O}_3$  can reversibly intercalate  $\text{Li}^+$  ions more than 4 mol, thereby providing a higher lithium storage capacity than that of commercial graphite anodes ( $372 \text{ mAh g}^{-1}$ ) [16]. However, the performance of iron oxide electrode is limited by the slow diffusion of  $\text{Li}$  ions and poor electrical conductivity of the electrode materials, resulting in rapid capacity fading with prolonged cycling [3,10]. Well-designed nanostructures can solve these problems by providing buffering space which can accommodate the volume expansion of electrode materials during charge–discharge processes. For instance, uniform hematite capsules showed the improved electrochemical performance (retained capacity of  $740 \text{ mAh g}^{-1}$  after 30 cycles) [17]. Nanoflakes of  $\alpha\text{-Fe}_2\text{O}_3$  were demonstrated as active anode materials with the stable capacity of ca.  $680 \text{ mAh g}^{-1}$  up to 80 cycles [18].

Another approach to overcome these problems is to wrap the active  $\text{Fe}_2\text{O}_3$  with carbon materials which can improve the electrochemical properties of the interface between electrodes and electrolytes: i) carbon coating, ii) carbon matrix embedding, iii) carbon-layer entanglement [19–22].  $\text{Fe}_3\text{O}_4$  nanospheres entangled with polyacrylic acid (PAA) exhibited greatly enhanced lithium storage properties with the retained capacity of  $712 \text{ mAh g}^{-1}$  after 60 cycles [20].  $\text{Fe}_3\text{O}_4$  nanoparticles embedded in graphene sheets also exhibited improved cycling stability and rate performance due to homogeneously dispersed  $\text{Fe}_3\text{O}_4$  (ca. 7 nm) in carbon matrix [22]. However, most of the synthetic procedures require complex steps with toxic chemicals under severe conditions.

In this work, carbon layer-entangled iron oxides were facilely prepared as active anode materials for Li-ion batteries through diamine-linked assembly of iron oxides and their subsequent heat-treatment at  $700 \text{ }^\circ\text{C}$  under  $\text{N}_2$  flow. The resulting nanocomposites exhibited the favorable nanostructure (i.e., iron oxide clusters entangled with conductive carbon layer) which can enhance the electrical conductivity and minimize the pulverization process, consequently leading to the improved electrochemical performance (e.g., high capacity retention and good cycling stability). The characteristic properties of as-prepared samples were analyzed by SEM (Scanning Electron Microscope), TEM (Transmission Electron Microscope), XRD (X-ray Diffraction), and the electrochemical properties of the samples were tested by cyclic voltammetry and galvanostatic cycling techniques.

## 2. Experimental

### 2.1. Preparation of citrate-capped magnetite clusters ( $\text{C-Fe}_3\text{O}_4$ )

Aqueous ferrofluid was prepared according to the modified co-precipitation method [23].  $\text{FeCl}_3$  and  $\text{FeCl}_2$  (3:2 mol ratio) were mixed with 25 ml of distilled water, and then 20 ml of ammonium hydroxide (28 wt%  $\text{NH}_3$ ) was quickly added into the mixture with vigorous stirring at room temperature. Black precipitates immediately formed and were mixed with 100 ml of citrate solution (1.0 M)

for 3 h at room temperature, then the mixture was refluxed for 1 h at  $70 \text{ }^\circ\text{C}$  to obtain citrate-capped magnetites ( $\text{C-Fe}_3\text{O}_4$ ).

### 2.2. Preparation of carbon-layered entangled iron oxides ( $\text{Fe}_2\text{O}_3@\text{carbon}$ )

Diamine molecules as a cross-linker were added to the  $\text{C-Fe}_3\text{O}_4$  solution to induce the cross-linked assembly of magnetite clusters. 1,12-diaminododecane (C-12 diamines of 1.0 M) was prepared by adding 2.0 g of C-12 diamines to 10 ml of aqueous solution. An aliquot volume (250  $\mu\text{l}$ , 1000  $\mu\text{l}$ ) of diamines was added into the  $\text{C-Fe}_3\text{O}_4$  solution and the mixed solution was stirred vigorously for 2 h at  $30 \text{ }^\circ\text{C}$ . Finally, diamine-linked magnetite clusters ( $\text{D-Fe}_3\text{O}_4$ ) were purified by removing residual impurities through several centrifugations. The  $\text{D-Fe}_3\text{O}_4$  was subsequently heat-treated under  $\text{N}_2$  flow at  $700 \text{ }^\circ\text{C}$  for 2 h, consequently leading to the formation of carbon layer-entangled iron oxide clusters ( $\text{Fe}_2\text{O}_3@\text{carbon}$ ).

### 2.3. Electrochemical measurements

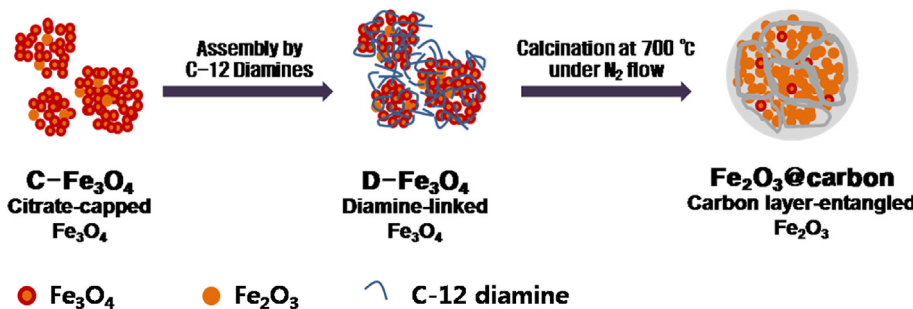
The half-cell electrodes for Li-ion batteries were described in other studies [24,25]. In preparing anode electrode materials, a slurry containing 70 wt% of magnetite powder, 15 wt% of denka black (DB) and 15 wt% of polyvinylidene fluoride (PVDF) dissolved in *N*-methyl-2-pyrrolidone (NMP) was pasted onto a Cu substrate. A half-cell assembled in a dry room with iron oxide composites was used as a working electrode, a metallic lithium foil as a counter electrode, 1.0 M  $\text{LiPF}_6$  in ethylene carbonate (EC), dimethyl carbonate (DMC), and ethylmethyl carbonate (EMC) as electrolytes, and a polypropylene-based film as a separator. The mass of working and Li counter electrode was 88.4 mg (including copper plate) and 80.9 mg, respectively. The loading densities of carbon free  $\text{Fe}_2\text{O}_3$  and  $\text{Fe}_2\text{O}_3@\text{carbon}$  were  $3.33 \times 10^{-3}$  and  $3.36 \times 10^{-3} \text{ g cm}^{-2}$ , respectively.

Cyclic voltammetry (CV) was measured in the voltage range between 0.05 V and 3.0 V at the scan rate of  $0.01 \text{ mV s}^{-1}$ . Galvanostatic discharge–charge cycling was measured at 0.1 C in the voltage range of 0.05–2.5 V.

## 3. Results and discussion

### 3.1. Nanocomposite preparation and its characterization

**Scheme 1** showed the fabrication procedures in which C-12 diamine acted as a cross-linker to assemble iron oxide clusters and the resulting composites were finally transformed into the  $\text{Fe}_2\text{O}_3@\text{carbon}$  through the heat-treatment process: (1) Diamine-linked magnetite clusters ( $\text{D-Fe}_3\text{O}_4$ ) were prepared by adding an aliquot volume of 1,12-diaminododecane (C-12 diamine of 1.0 M) into citrate-capped  $\text{Fe}_3\text{O}_4$  ( $\text{C-Fe}_3\text{O}_4$ ) solution prepared by the co-



**Scheme 1.** Fabrication schemes for carbon-layer entangled iron oxides.

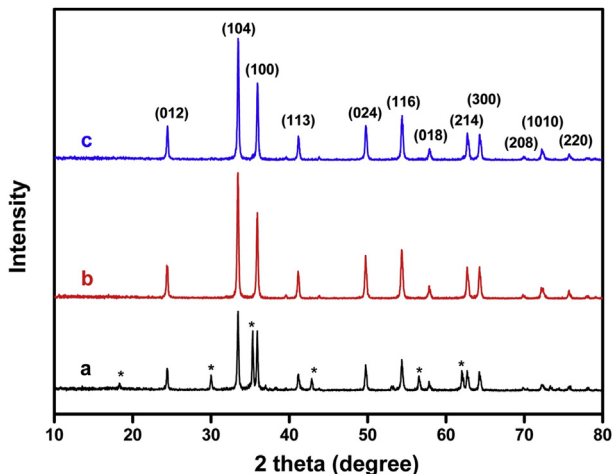


**Fig. 1.** XRD patterns of as-prepared samples calcined under  $N_2$  flow at  $700\text{ }^\circ\text{C}$  for 2 h: (a) C- $\text{Fe}_3\text{O}_4$ , (b) D- $\text{Fe}_3\text{O}_4$  (250  $\mu\text{l}$  of diamines), (c) D- $\text{Fe}_3\text{O}_4$  (1000  $\mu\text{l}$  of diamines). The asterisks represent the XRD peaks of  $\text{Fe}_3\text{O}_4$  in a sequential order: (111), (220), (311), (400), (511), and (440).

precipitation method; (2) The C-12 diamine played as a molecular cross-linker to transform the C- $\text{Fe}_3\text{O}_4$  into diamine-linked iron oxide clusters (D- $\text{Fe}_3\text{O}_4$ ); (3) The resulting D- $\text{Fe}_3\text{O}_4$  was subsequently heat-treated at  $700\text{ }^\circ\text{C}$  under  $N_2$  flow, finally forming carbon-layer entangled iron oxide clusters ( $\text{Fe}_2\text{O}_3@\text{carbon}$ ). In Scheme 1, the initial C- $\text{Fe}_3\text{O}_4$  samples were depicted with coexisting dominant fraction of  $\text{Fe}_3\text{O}_4$  with red circle (in Web version) and small fraction of  $\text{Fe}_2\text{O}_3$  with orange color, probably due to the partial formation of  $\text{Fe}_2\text{O}_3$  during the co-precipitation process [26].

The crystalline structures of as-prepared samples were characterized by X-ray powder diffraction (XRD; Rigaku Corp.,  $\text{Cu}\text{k}\alpha = 40\text{ kV }50\text{ mA, } \lambda = 2^\circ\text{ min}^{-1}$ ). Typical XRD patterns of iron oxide composites (heat treatment at  $700\text{ }^\circ\text{C}$  under  $N_2$  flow) are shown in Fig. 1. While uncalcined C- $\text{Fe}_3\text{O}_4$  exhibited the XRD patterns

corresponding to the face-centered cubic (fcc)  $\text{Fe}_3\text{O}_4$  (data not shown), the diffraction peaks of calcined C- $\text{Fe}_3\text{O}_4$  represented the black line (a) showing the mixture of face-centered cubic (fcc)  $\text{Fe}_3\text{O}_4$  ( $2\theta = 30.4^\circ, 35.6^\circ, 43.3^\circ, 57.5^\circ$ ) and hexagonal phase of  $\alpha\text{-Fe}_2\text{O}_3$  ( $2\theta = 24.1^\circ, 33.44^\circ, 41.12^\circ, 49.72^\circ, 54.38^\circ, 62.7^\circ$ ) [19]. The red and blue lines of calcined D- $\text{Fe}_3\text{O}_4$  (250  $\mu\text{l}$  and 1000  $\mu\text{l}$  of diamines) show diffraction peaks attributed to standard hexagonal phase of  $\alpha\text{-Fe}_2\text{O}_3$ , indicating the phase transformation of  $\text{Fe}_3\text{O}_4$  to hematite crystals ( $\alpha\text{-Fe}_2\text{O}_3$ ) during the calcinations process [13,19]. According to Figure S1 (in Supplemental Information), the saturated magnetism of calcined D- $\text{Fe}_3\text{O}_4$  was negligibly small (ca. 0.5–1.0  $\text{emu g}^{-1}$ ), which was the characteristic value of  $\alpha\text{-Fe}_2\text{O}_3$ . On the other hand, the calcined C- $\text{Fe}_3\text{O}_4$  at  $700\text{ }^\circ\text{C}$  exhibited the fair magnetism caused by residual  $\text{Fe}_3\text{O}_4$  (or  $\gamma\text{-Fe}_2\text{O}_3$ ) due to the partial transformation of  $\text{Fe}_3\text{O}_4$  into  $\alpha\text{-Fe}_2\text{O}_3$  [27–29].

The scanning electron microscopy (SEM) image was taken on a HITACHI S-4700 scanning microscope using an accelerating voltage of 15 kV. Fig. 2a showed the SEM image of uncalcined C- $\text{Fe}_3\text{O}_4$  showing the aggregated form of primary  $\text{Fe}_3\text{O}_4$  nanoparticles (ca. 15 nm). The calcined C- $\text{Fe}_3\text{O}_4$  exhibited a relatively large and heterogeneous cuboid surface morphology as shown in Fig. 2b, indicating the crystal phase transition from  $\text{Fe}_3\text{O}_4$  to  $\text{Fe}_2\text{O}_3$  crystals during the heat-treatment process. According to Fig. 2c, the calcined D- $\text{Fe}_3\text{O}_4$  (250  $\mu\text{l}$  of diamines) exhibited the clustered form of iron oxides (ca. 500 nm), and the calcined D- $\text{Fe}_3\text{O}_4$  (1000  $\mu\text{l}$  of diamines) exhibited the heavily agglomerated iron oxides as shown in Fig. 2d. The inset shown in Fig. 2c was the corresponding TEM image of carbon-layer entangled iron oxide clusters. HRTEM (HITACHI, H7600) of calcined D- $\text{Fe}_3\text{O}_4$  (250  $\mu\text{l}$  of diamines), so called  $\text{Fe}_2\text{O}_3@\text{carbon}$  (250  $\mu\text{l}$  of diamines), clearly revealed the atomic lattice fringes (0.25 nm) of crystalline  $\text{Fe}_2\text{O}_3$  interfaced with distinct carbon layer (ca. 5 nm) (see Fig. 2e) [15]. Fig. 2f showed the SAED of  $\text{Fe}_2\text{O}_3@\text{carbon}$  (250  $\mu\text{l}$  of diamines) in which the distinct diffractive rings were attributable to crystalline iron oxides.

To confirm the porous nanostructure, a nitrogen adsorption–desorption measurement was conducted to characterize the BET surface area and internal pore structure. According to Fig. 3, the

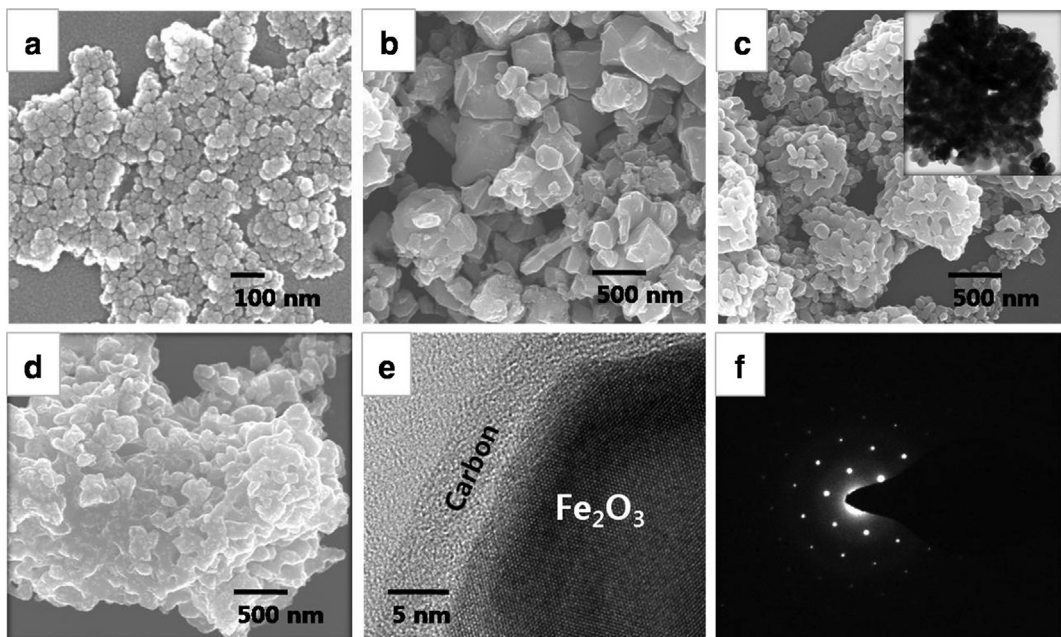


**Fig. 2.** SEM images of as-prepared samples: (a) Uncalcined C- $\text{Fe}_3\text{O}_4$ , (b) Calcined C- $\text{Fe}_3\text{O}_4$ , (c) Calcined D- $\text{Fe}_3\text{O}_4$  (250  $\mu\text{l}$  of diamines), (d) Calcined D- $\text{Fe}_3\text{O}_4$  (1000  $\mu\text{l}$  of diamines), (e) HR-TEM of calcined D- $\text{Fe}_3\text{O}_4$  (250  $\mu\text{l}$  of diamines), (f) SAED of  $\alpha\text{-Fe}_2\text{O}_3@\text{carbon}$  (250  $\mu\text{l}$  of diamines). The inset shown in 2c indicates the TEM image of calcined D- $\text{Fe}_3\text{O}_4$  (250  $\mu\text{l}$  of diamines). The calcined C- $\text{Fe}_3\text{O}_4$  and D- $\text{Fe}_3\text{O}_4$  represent carbon free  $\text{Fe}_2\text{O}_3$  and  $\text{Fe}_2\text{O}_3@\text{carbon}$ , respectively.

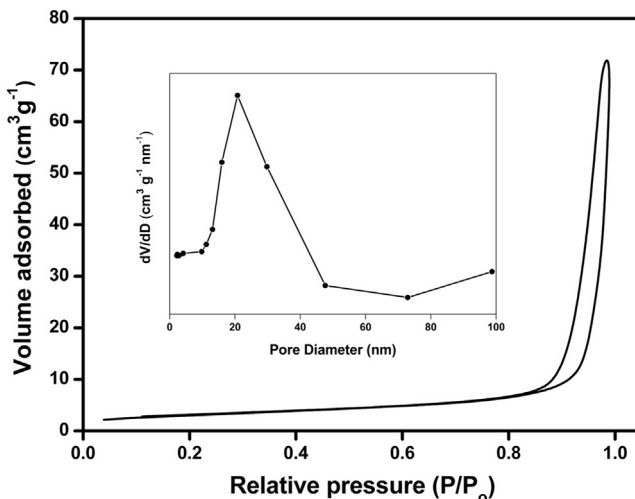


Fig. 3. Nitrogen adsorption–desorption isotherms with corresponding BJH desorption pore size distributions (inset) of  $\text{Fe}_2\text{O}_3$ @carbon (250  $\mu\text{l}$  of diamines).

adsorption–desorption curve of  $\text{Fe}_2\text{O}_3$ @carbon (250  $\mu\text{l}$  of diamines) was classified as type III isotherm without a distinct hysteresis loop, implicating the existence of some amounts of mesoporosity [20,29–31]. The surface area of  $\text{Fe}_2\text{O}_3$ @carbon

(250  $\mu\text{l}$  of diamines) was calculated as  $10.96 \text{ m}^2 \text{ g}^{-1}$ , while the surface area of carbon free  $\text{Fe}_2\text{O}_3$  was calculated as  $4.23 \text{ m}^2 \text{ g}^{-1}$ . The inset of Fig. 3 showed the BJH desorption pore size distribution of  $\text{Fe}_2\text{O}_3$ @carbon showing a dominant mesopore peak around 20 nm, mainly attributed to secondary interspaces between iron oxide clusters caused by carbon-layer entanglement. On the other hand, the carbon free  $\text{Fe}_2\text{O}_3$  exhibited the pore size distribution of a sharp peak at 3.5 nm and a weakly broad peak at around 20 nm (see Figure S2 in Supplementary Information). The large specific surface area and high porosity of iron oxides can facilitate the diffusion of Li ions, which will enhance the electrochemical performance of  $\text{Fe}_2\text{O}_3$ @carbon electrode in comparison to carbon free  $\text{Fe}_2\text{O}_3$  electrode.

### 3.2. Electrochemical properties of the nanocomposite

The electrochemical properties of as-prepared composites were tested as anode materials for Li-ion batteries. Fig. 4a and b showed the initial five cycles of carbon free  $\text{Fe}_2\text{O}_3$  (calcined C- $\text{Fe}_3\text{O}_4$ ) and  $\text{Fe}_2\text{O}_3$ @carbon (calcined D- $\text{Fe}_3\text{O}_4$ ) at 0.1 C. For the first cycle of both samples, large irreversible capacity was observed due to the formation of a solid–electrolyte interface (SEI), irreversible  $\text{Li}_2\text{O}$  formation, and/or the phase transition of electrodes [14,16,22]. The initial discharge capacity of carbon free  $\text{Fe}_2\text{O}_3$  and  $\text{Fe}_2\text{O}_3$ @carbon (250  $\mu\text{l}$  of diamines) were 1260 and 1094 mAh  $\text{g}^{-1}$ , respectively,

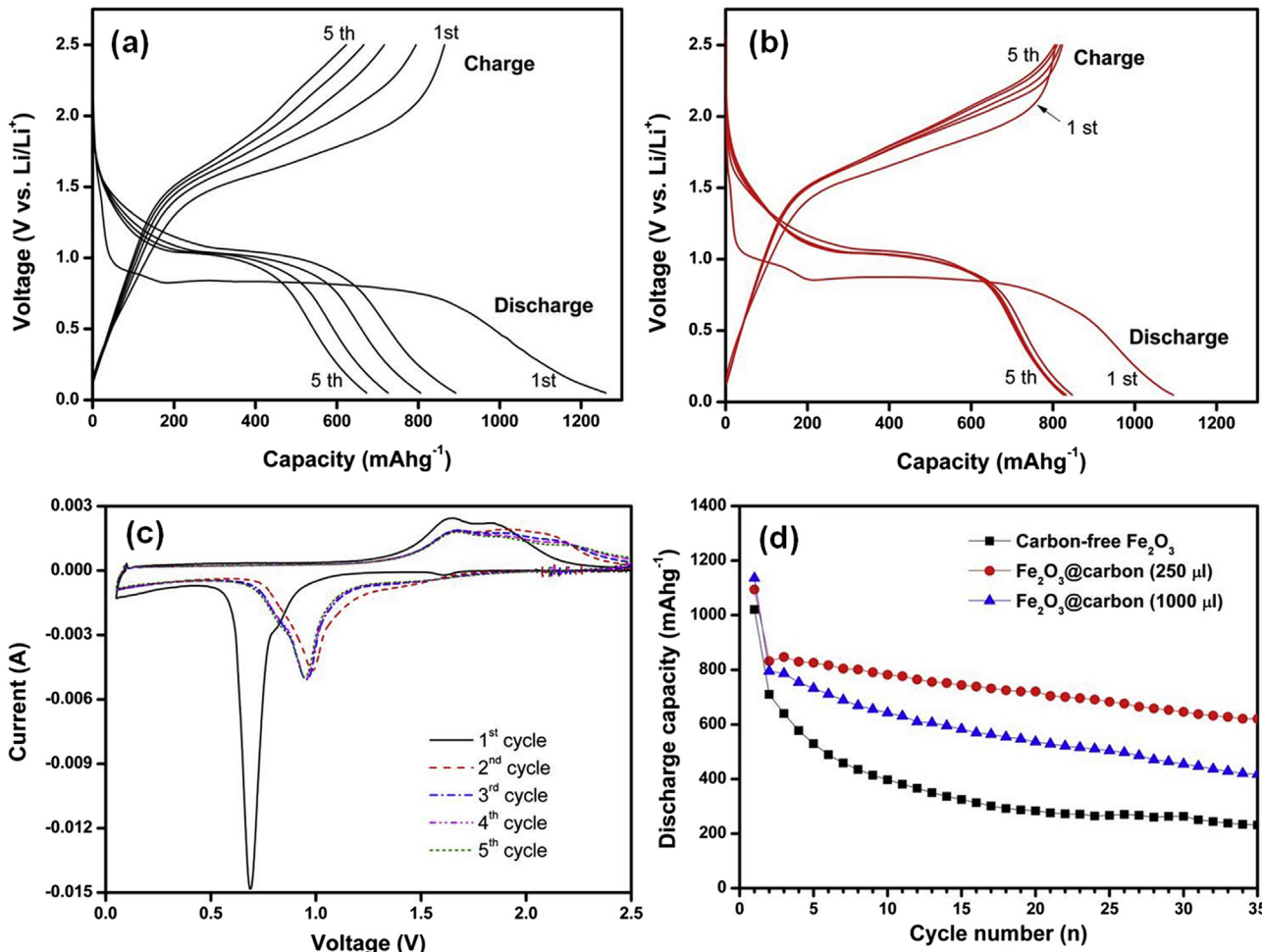


Fig. 4. Discharge and charge profiles of (a) carbon free  $\text{Fe}_2\text{O}_3$ , (b)  $\text{Fe}_2\text{O}_3$ @carbon (250  $\mu\text{l}$  of diamines), and (c) cyclic voltammetry curves of  $\text{Fe}_2\text{O}_3$ @carbon (250  $\mu\text{l}$  of diamines) measured between 0.01 and 2.5 V at the scan rate of 0.1 mV  $\text{s}^{-1}$ , (d) Galvanostatic cycling performance of the iron oxide composites at 0.1 C.

which resulted in 68.6% and 73.7% of coulombic efficiency in the first cycle. In the second cycle, the coulombic efficiency of carbon free  $\text{Fe}_2\text{O}_3$  and  $\text{Fe}_2\text{O}_3@\text{carbon}$  (250  $\mu\text{l}$  of diamines) was raised up to 90.8% and 98.2%, respectively. In the discharge curve of  $\text{Fe}_2\text{O}_3@\text{carbon}$  (250  $\mu\text{l}$  of diamines) shown in Fig. 4b, there was a weak potential slope located at 1.2–1.0 V and an obvious potential plateau at 0.75 V, corresponding to the reduction of Fe ions to  $\text{Fe}^0$  and the formation of amorphous  $\text{Li}_2\text{O}$ , respectively [32]. In the subsequent cycles, only one discharge slope was observed in the range of 1.2–1.0 V with a slight decrease of the discharge capacity of  $\text{Fe}_2\text{O}_3@\text{carbon}$  [7,13].

Cyclic voltammetry (CV) curves of  $\text{Fe}_2\text{O}_3@\text{carbon}$  were obtained in the voltage range between 0.01 and 2.5 V at the scan rate of 0.1  $\text{mV s}^{-1}$  (see Fig. 4c). In the first cycle of a cathodic processing,  $\text{Fe}_3\text{O}_4@\text{carbon}$  (250  $\mu\text{l}$  of diamines) exhibited one spiky peak at around 0.7 V, which was shifted to higher potential of ca. 0.95 V in the second cycle. This can be attributed to the reduction of  $\text{Fe}^{3+}$  to  $\text{Fe}^0$  (lithium insertion) and some irreversible reaction with the electrolytes [20]. In the subsequent cycles, the cathodic peak kept almost constant, indicating the good reversibility of the reduction process in  $\text{Fe}_2\text{O}_3@\text{carbon}$  (250  $\mu\text{l}$  of diamines). A broad anodic peak was observed at the potential of 1.6–1.8 V corresponding to the oxidation of  $\text{Fe}^0\text{--Fe}^{3+}$  (lithium extraction) [13,21]. The two peaks observed in the anodic processing can be attributed to a change in iron oxide oxidation states in two steps, i.e.,  $\text{Fe}^0\text{--Fe}^{2+}$  at 1.7 V and  $\text{Fe}^{2+}\text{--Fe}^{3+}$  at 1.85 V [22]. In the subsequent cycles, the anodic peak for  $\text{Fe}_2\text{O}_3@\text{carbon}$  was kept almost constant, indicating that the electrochemical reaction has proceeded to a similar extent.

The cycling performance of as-prepared samples was evaluated at 0.1 C in the voltage window of 0.05–2.5 V vs. Li (see Fig. 4d). Carbon free  $\text{Fe}_2\text{O}_3$  exhibited a rapid capacity fading, retaining only 22% of the initial capacity after 35 cycles. On the other hand, the retaining capacity of  $\text{Fe}_2\text{O}_3@\text{carbon}$  (250  $\mu\text{l}$  of diamines) and  $\text{Fe}_2\text{O}_3@\text{carbon}$  (1000  $\mu\text{l}$  of diamines) was 56% and 40% after 35 cycles, respectively. The  $\text{Fe}_2\text{O}_3@\text{carbon}$  (250  $\mu\text{l}$  of diamines) exhibited the improved capacity retention by ca. 150% as compared to that of the carbon free  $\text{Fe}_2\text{O}_3$ . Even though it would be difficult to separate the contributions from more carbon layer or carbon matrix structural effects, carbon layer on iron oxides evidently contributed to the improved cycling performance due to the enhanced conductivity of iron oxides [7,19–22].

The carbon-layer entanglement also contributed to the improved cycling performance of the  $\text{Fe}_2\text{O}_3@\text{carbon}$  electrode by playing as a buffering matrix during charging/discharging process [20]. According to Figure S3 (in Supplemental Information) showing the morphological changes of the electrode after cycling, the carbon free  $\text{Fe}_2\text{O}_3$  electrode showed more cracked surface than that of the  $\text{Fe}_2\text{O}_3@\text{carbon}$  electrode. The  $\text{Fe}_2\text{O}_3@\text{carbon}$  electrode exhibited less cracked surface and more connected structural integrity after cycling. These experimental results highlighted the benefits of entangled carbon layer which could accommodate the volume expansion and keep the structural integrity of the electrode during cycling [33,34].

The rate capability of  $\text{Fe}_2\text{O}_3@\text{carbon}$  (250  $\mu\text{l}$  of diamines) at variable current rates was presented in Fig. 5. The initial capacity of 815, 690, 530, 331  $\text{mAh g}^{-1}$  was observed when the current rate increased from 0.1 C to 0.25, 0.5, 1.0 C, respectively. When the rate returned to the initial 0.1 C, the composite electrode regained the original capacity more than 700  $\text{mAh g}^{-1}$ , demonstrating the reversibility of the iron oxide composites [17,31,35]. Even though somewhat rapid capacity fading was observed at higher current rates, the composite electrode can be a promising candidate for high power applications if stronger cross-linkers are employed, such as polyamine or chitosan polymers which can effectively entangle iron oxide particles with surface carboxylate groups [18].

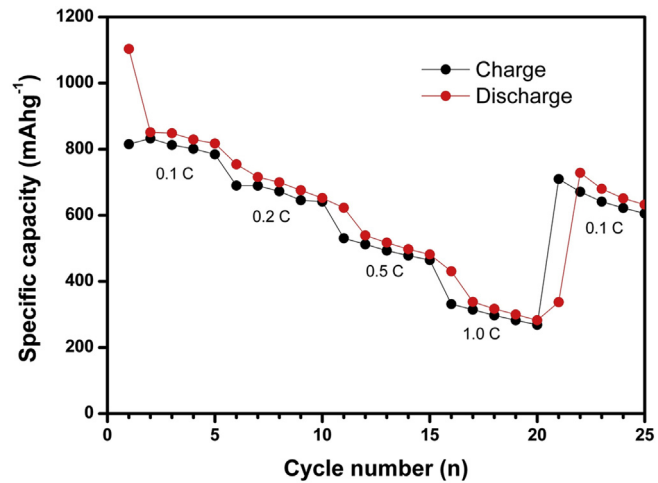


Fig. 5. Rate performance of  $\text{Fe}_2\text{O}_3@\text{carbon}$  (250  $\mu\text{l}$  of diamines) at variable C rates.

#### 4. Conclusions

In this work, carbon layer-entangled iron oxides ( $\text{Fe}_2\text{O}_3@\text{carbon}$ ) were facilely prepared through the cross-linking assembly of iron oxides induced by the addition of C-12 diamines (1,12-diaminododecane). The resulting composites after heat-treatment at 700 °C under  $\text{N}_2$  flow exhibited the XRD patterns mainly corresponding to hexagonal phase of hematite ( $\alpha\text{-Fe}_2\text{O}_3$ ) with negligible magnetism. The  $\text{Fe}_2\text{O}_3@\text{carbon}$  (250  $\mu\text{l}$  of diamines) exhibited good capacity retention capability, due to the improved electrical conductivity and structural integrity by the entangled carbon layer. However, the excessive addition of diamines (1000  $\mu\text{l}$ ) led to a somewhat rapid capacity fading of the composite electrode. Thus, it is beneficial to prepare the optimal carbon layer-entangled iron oxides for improved Li-ion batteries, suggesting a useful guideline when coating conductive carbon on transition metal oxides with high pulverization rates.

#### Acknowledgments

This work was supported by the National Research Foundation of Korea Grant funded by the Korean Government (MEST) (NRF-2010-C1AAA001-2010-0028958).

#### Appendix A. Supplementary data

Supplementary data related to this article can be found at <http://dx.doi.org/10.1016/j.jpowsour.2013.01.120>.

#### References

- [1] K. Ozawa, Solid State Ionics 69 (1994) 212–221.
- [2] Y.G. Guo, Y.S. Hu, W. Sigle, J. Maier, Adv. Mater. 19 (2007) 2087–2091.
- [3] P. Poizot, S. Laruelle, S. Grangeon, L. Dupont, J.-M. Tarascon, Nature 407 (2000) 496–499.
- [4] C.K. Chan, H. Peng, G. Liu, K. Mcilwrath, X.F. Zhang, R.A. Huggins, Y. Cui, Nat. Nanotechnol. 3 (2008) 31–35.
- [5] J.M. Tarascon, M. Armand, Nature 414 (2001) 359–367.
- [6] W.Y. Li, L.N. Xu, J. Chen, Adv. Funct. Mater. 15 (2005) 851–857.
- [7] H. Liu, G. Wang, J. Wang, D. Wexler, Electrochim. Commun. 10 (2008) 1879–1882.
- [8] J. Li, H.M. Dahn, L.J. Krause, D.B. Le, J.R. Dahn, J. Electrochem. Soc. 155 (2008) A812–A816.
- [9] J. Gao, J. Li, X. He, C. Jiang, C. Wan, Int. J. Electrochim. Sci. 6 (2011) 2818–2825.
- [10] W.M. Zhang, X.L. Wu, J.S. Hu, Y.G. Guo, L.J. Wan, Adv. Funct. Mater. 18 (2008) 3941–3946.
- [11] H. Li, P. Balaya, J. Maier, J. Electrochim. Soc. 151 (2004) A1878–A1885.
- [12] P.L. Taberna, S. Mitra, P. Poizot, P. Simon, J.M. Tarascon, Nat. Mater. 5 (2006) 567–573.

[13] Y. NuLi, R. Zeng, P. Zhang, Z. Guo, H. Liu, *J. Power Sources* 184 (2008) 456–461.

[14] S. Zeng, K. Tang, T. Li, Z. Liang, D. Wang, Y. Wang, Y. Qi, W. Zhou, *J. Phys. Chem. C* 112 (2008) 4836–4843.

[15] X. Zhu, Y. Zhu, S. Murali, M.D. Stoller, R.S. Ruoff, *ACS Nano* 5 (2011) 3333–3338.

[16] J. Chen, L.N. Xu, W.Y. Li, X.L. Gou, *Adv. Mater.* 17 (2005) 582–586.

[17] S. Jin, H. Deng, D. Long, X. Liu, L. Zhan, X. Liang, W. Qiao, L. Ling, *J. Power Sources* 196 (2011) 3887–3893.

[18] J.S. Chen, Y. Zhang, X.W. Lou, *ACS Appl. Mater. Interfaces* 3 (2011) 3276–3279.

[19] D. Chen, G. Ji, Y. Ma, J.Y. Lee, J. Lu, *ACS Appl. Mater. Interfaces* 3 (2011) 3078–3083.

[20] J. Su, M. Cao, L. Ren, C. Hu, *J. Phys. Chem. C* 115 (2011) 14469–14477.

[21] H.S. Kim, Y. Piao, S.H. Kang, T. Hyeon, Y. Sung, *Electrochem. Commun.* 12 (2010) 382–385.

[22] M.V. Reddy, T. Yu, C. Sow, Z.X. Shen, C.T. Lim, G.V.S. Rao, B.V.R. Chowdari, *Adv. Funct. Mater.* 17 (2007) 2792–2799.

[23] S. Lim, D. Yang, S. Lee, *J. Nanosci. Nanotechnol.* 10 (2010) 7295–7299.

[24] B. Kim, S. Park, J. Lim, J. Lee, *Phys. Scr.* T139 (2010) 014027.

[25] S. Park, B. Kim, S. Lee, J. Lee, *Trans. Nonferrous Met. Soc. China* 19 (2009) 1023–1026.

[26] S. Laurent, D. Forge, M. Port, A. Roch, C. Robic, L.V. Elst, R.N. Muller, *Chem. Rev.* 108 (2008) 2064–2110.

[27] N. Pinnia, S. Grancharov, P. Beato, P. Bonville, M. Antonietti, M. Niederberger, *Chem. Mater.* 17 (2005) 3044–3049.

[28] W. Wu, Q. He, C. Jiang, *Nanoscale Res. Lett.* 3 (2008) 397–415.

[29] S.K. Behera, *J. Power Sources* 196 (2011) 8669–8674.

[30] P.G. Bruce, B. Scrosati, J.M. Tarascon, *Angew. Chem. Int. Ed.* 47 (2008) 2930–2946.

[31] Q.Q. Xiong, J.P. Tu, Y. Lu, J. Chen, Y.X. Yu, Y.Q. Qiao, X.L. Wang, C.D. Gu, *J. Phys. Chem. C* 116 (2012) 6495–6502.

[32] Z. Cui, L. Jiang, W. Song, Y. Guo, *Chem. Mater.* 21 (2011) 1162–1166.

[33] Y. Zou, J. Kan, Y. Wang, *J. Phys. Chem. C* 115 (2011) 20747–20753.

[34] X. Li, X. Huang, D. Liu, X. Wang, S. Song, L. Zhou, H. Zhang, *J. Phys. Chem. C* 115 (2011) 1567–21573.

[35] J. Liu, Y. Li, H. Fan, Z. Zhu, J. Jiang, R. Ding, Y. Hu, X. Huang, *Chem. Mater.* 22 (2011) 212–217.